POLITECNICO DI TORINO
Repository ISTITUZIONALE

CompositionDependent Solvation in LowConcentration MultiSalt DME Electrolytes: Correlations With Lithium Deposition and Interfacial Evolution

Original
CompositionDependent Solvation in LowConcentration MultiSalt DME Electrolytes: Correlations With Lithium Deposition and Interfacial Evolution / Gentile, A., Moreno, M., Falconieri, M., Monconduit, L., Stievano, L., Brutti, S.. - In: CHEMELECTROCHEM. - ISSN 2196-0216. - 13:21(2026), pp. 1-16. [10.1002/celc.70331]

Availability:
This version is available at: 11583/3017124 since: 2026-11-02T17:12:12Z

Publisher:
John Wiley and Sons

Published
DOI:10.1002/celc.70331

Terms of use:

This article is made available under terms and conditions as specified in the corresponding bibliographic description in the repository

Publisher copyright

(Article begins on next page)

27 November 2026

Check for updates

ChemElectroChem

Chemistry Europe
European Chemical Societies Publishing
ChemElectroChem

RESEARCH ARTICLE OPEN ACCESS

Composition-Dependent Solvation in Low-Concentration Multi-Salt DME Electrolytes: Correlations With Lithium Deposition and Interfacial Evolution

Andrea Gentile[1,2,3] | Margherita Moreno[2] | Mauro Falconieri[4] | Laure Monconduit[3,5,6] | Lorenzo Stievano[3,5,6,7] | Sergio Brutti[1,5,8,9]

[1]Department of Chemistry, Sapienza University of Rome, Rome, Italy | [2]Energy Technologies and Renewable Sources Department, ENEA, C.R. Casaccia, Rome, Italy | [3]ICGM, CNRS, ENSCM, Univ. Montpellier, Montpellier, France | [4]Nuclear Department, ENEA, C.R. Casaccia, Rome, Italy | [5]ALISTORE European Research Institute (ALISTORE ERI), CNRS, Amiens, France | [6]RS2E, Réseau sur le Stockage Electrochimique de l'Energie, CNRS, Amiens, France | [7]GAME Lab, Department of Applied Science and Technology (DISAT), Politecnico di Torino, Torino, Italy | [8]GISEL Centro di Riferimento Nazionale per i Sistemi di Accumulo Elettrochimico di Energia, Florence, Italy | [9]Istituto dei Sistemi Complessi, Consiglio Nazionale delle Ricerche, Rome, Italy

Correspondence: Lorenzo Stievano (lorenzo.stievano@umontpellier.fr) | Sergio Brutti (sergio.brutti@uniroma1.it)

Received: 3 August 2026 | **Revised:** 29 September 2026 | **Accepted:** 5 October 2026

Keywords: electrolyte solvation | lithium deposition | lithium metal battery | multi-salt electrolytes | solid–electrolyte interphase

ABSTRACT

Lithium metal battery behavior is strongly influenced by the electrolyte environment from which the solid–electrolyte interphase develops, yet the effects of combining anions in dilute multi-salt formulations remain incompletely understood. Combinations of LiFSI, LiTFSI, and $LiNO_3$ in DME, at a total Li^+ concentration of 1 mol kg^{-1}, were investigated using complementary spectroscopy, electrochemistry, and microscopy. Raman and $^1H/^7Li$ NMR spectroscopy reveal composition-dependent changes in imide-anion association, DME coordination-sensitive spectral features, and the average Li^+ environment. These changes are accompanied by interfacial impedance responses and lithium deposit morphologies. Most notably, all nitrate-containing formulations show improved preservation of a lithium reservoir formed on Cu, sustaining 80–86 reversible cycles with average Coulombic efficiencies close to 99%, while displaying limited impedance evolution and more continuous deposits. Within this nitrate-containing series, FSI and TFSI produce distinct spectroscopic and interfacial responses, even though a ranking in reservoir reversibility cannot be established. TFSI is shifted predominantly toward noncontact environments upon nitrate addition, whereas FSI retains a substantial contribution from contact-associated configurations. The combined results demonstrate that multi-salt electrolytes cannot be described as simple superpositions of their single-salt components and support a working interpretation in which the anion composition modulates the prereduction Li^+ solvation ensemble and subsequent interfacial evolution.

1 | Introduction

The growing electrification of transportation and the increasing deployment of renewable energy infrastructures continue to drive the development of electrochemical energy storage systems with higher energy density, longer lifetimes, and improved sustainability [1]. Although conventional lithium-ion batteries have enabled the rapid development of portable electronics and electric vehicles, their energy density is approaching the practical limits imposed by graphite-based negative electrodes [2]. Further improvements in battery performance therefore require the adoption of alternative electrode chemistries capable of storing larger amounts of lithium while minimizing the fraction of electrochemically inactive materials within the cell [3, 4].

This is an open access article under the terms of the Creative Commons Attribution License, which permits use, distribution and reproduction in any medium, provided the original work is properly cited.

© 2026 The Author(s). *ChemElectroChem* published by Wiley-VCH GmbH.

Among all candidate anode materials, lithium metal is widely regarded as the ultimate negative electrode because of its exceptionally high theoretical specific capacity (3860 mAh g^{-1}), low density (0.534 g cm^{-3}), and the most negative electrochemical potential among practical electrode materials (−3.04 V vs. the standard hydrogen electrode) [5]. These characteristics make lithium metal particularly attractive for next-generation battery technologies based on high-capacity cathodes and, most importantly, for so-called zero-excess (anode-free) lithium metal batteries (ZE-LMBs) [6–8]. In these architectures, the cell is assembled without a lithium metal anode, and all cyclable lithium is initially stored within the cathode. During the first charge, lithium is plated directly onto a bare current collector, creating the active lithium reservoir required for subsequent cycling [9]. By eliminating excess lithium and host-anode materials, this configuration maximizes the practical energy density of the device and represents one of the most promising routes toward battery systems exceeding 400 Wh kg^{-1} [10].

The absence of excess lithium, however, introduces a fundamental challenge [11]. Because the total lithium inventory is strictly limited, every irreversible side reaction directly consumes active lithium and permanently reduces the cell capacity. Consequently, the long-term viability of zero-excess cells depends critically on the reversibility of lithium plating and stripping during the earliest stages of cell operation [12]. The initial lithium deposition on the bare support surface is particularly important [13] as it establishes both the morphology of the lithium reservoir and the initial solid–electrolyte interphase (SEI), which together determine the subsequent evolution and stability of the interface [14, 15]. Morphological instabilities may lead to the formation of electrically disconnected "dead" lithium [16, 17], while continuous electrolyte decomposition promotes SEI growth and progressive lithium consumption [18]. These degradation mechanisms remain among the principal obstacles preventing the practical implementation of ZE-LMBs.

Over the past decade, substantial efforts have therefore been devoted to electrolyte engineering as a means of controlling lithium deposition and stabilizing the SEI [19–25]. A broad body of literature has demonstrated that the structure of the primary Li^+ solvation shell strongly influences the reduction pathways occurring at the electrode surface and, consequently, the composition and properties of the resulting SEI [26]. This understanding has led to the development of highly concentrated electrolytes [19], localized high-concentration electrolytes [27–29], fluorinated solvent systems [30, 31], and a wide range of electrolyte additives designed to promote inorganic-rich interphases [32–39], while weakly solvating electrolytes have been developed to increase anion participation in the Li^+ coordination environment at conventional salt concentrations by limiting the coordinating ability of the solvent [40, 41]. More generally, recent work has emphasized that electrolyte behavior cannot be described solely in terms of cation–solvent coordination: cation–anion, anion–solvent, solvent–solvent, and higher-order interactions collectively determine ion association, transport, desolvation, and interfacial chemistry [42]. In particular, both anion–solvent interactions and cation–anion solvation engineering have been shown to provide additional degrees of freedom for tuning electrolyte properties beyond conventional solvent-centered descriptions [43, 44].

This broader picture is especially relevant to multi-salt electrolytes, in which several anions with different coordinating and interphase-forming tendencies coexist within the same liquid phase. Lithium salt anions, like bis(fluorosulfonyl)imide (FSI), bis(trifluoromethanesulfonyl)imide (TFSI), and nitrate (NO_3^-), provide representative examples. FSI-based electrolytes, for example, can generate lithium fluorine-rich (LiF) SEIs with favorable passivation properties [45], whereas nitrate-containing formulations promote nitrogen-containing interphases comprising lithium nitride (Li_3N) and lithium nitrogen oxides (LiN_xO_y) species [11]. TFSI-based electrolytes, in turn, offer high oxidative stability and compatibility with high-voltage cathodes [46]. Combining salts containing these anions has therefore been explored as a route to improve lithium plating/stripping reversibility, deposit morphology, and cycling stability [47–62].

The behavior of such mixtures, however, cannot necessarily be inferred by superimposing the properties of the individual salts. Changing the relative abundance and identity of the anions modifies not only the number of potentially reducible species but also the ion association equilibria and the average Li^+ solvation environment. Recent molecular dynamics and experimental investigations of mixed LiTFSI/$LiNO_3$ glyme electrolytes, for example, have shown that varying the ratio between weakly associating TFSI and more strongly associating NO_3^- substantially modifies both solvation structure and dynamics [63]. Nevertheless, establishing such effects experimentally remains challenging because most spectroscopic observables are ensemble averaged and do not uniquely identify the complete molecular composition of the primary Li^+ coordination shell. Moreover, comparatively little is known about how composition among coexisting anions may modify Li^+ solvation in dilute multi-salt electrolytes and how this correlates with the formation and stability of lithium deposited on a current collector.

The present work addresses this question through a systematic investigation of low-concentration, multi-salt ether electrolytes based on LiFSI, LiTFSI, and/or $LiNO_3$ dissolved in 1,2-dimethoxyethane (DME). Binary and ternary formulations were prepared while maintaining a constant total Li^+ molality of 1 mol kg^{-1}, allowing the effects of anion identity and combination to be compared without simultaneously changing the total salt content. A modified Aurbach protocol [64–66] was used to form and repeatedly cycle a finite lithium reservoir on bare copper substrates against a lithium metal counter electrode (CE). This Cu||Li configuration is used here as a controlled model for investigating the electrolyte-dependent processes governing the formation and stability of the lithium interface, establishing a rational basis for the development of advanced multi-salt electrolyte formulations. Two- and three-electrode measurements, electrochemical impedance spectroscopy (EIS), ex situ optical and electron microscopy, Raman spectroscopy, and $^1H/^7Li$ NMR were combined to correlate electrolyte composition with ion solvation/association, average Li^+/DME environments, interfacial evolution, and lithium morphology.

The results reveal two principal composition-dependent effects: First, the nitrate-containing formulations are clearly distinguished from the nitrate-free electrolytes by their markedly improved preservation of the lithium reservoir, more limited evolution of the working electrode (WE) impedance

21960216, 2026, 21, Downloaded from https://chemistry-europe.onlinelibrary.wiley.com/doi/10.1002/celc.70331 by Politecnico Di Torino Sist. Bibl Del Polit Di Torino, Wiley Online Library on [02/11/2026]. See the Terms and Conditions (https://onlinelibrary.wiley.com/terms-and-conditions) on Wiley Online Library for rules of use; OA articles are governed by the applicable Creative Commons License

during partial stripping, and more continuous lithium deposits. Second, substantial spectroscopic differences remain within the nitrate-containing series: Raman spectroscopy shows that TFSI is shifted toward predominantly noncontact environments in the presence of $LiNO_3$, whereas FSI retains a significant contribution from contact-associated configurations. These differences are accompanied by composition-dependent changes in the DME Raman response and in the average ^{7}Li and ^{1}H NMR environments but do not produce clearly distinguished differences in lithium reservoir reversibility. Taken together, these observations demonstrate that the behavior of multi-salt electrolytes is nonadditive and support a working interpretation in which the complete anion composition modulates the prereduction Li^+ solvation ensemble and, as a consequence, the subsequent interfacial evolution.

2 | Experimental Section

2.1 | Electrolyte Preparation and Electrochemical Cell Assembly

Lithium bis(fluorosulfonyl)imide (LiFSI, Sigma-Aldrich) was used as received from the supplier. Lithium bis(trifluoromethanesulfonyl)imide (LiTFSI, Sigma-Aldrich) and lithium nitrate ($LiNO_3$, Sigma-Aldrich) were dried at 120 °C overnight prior to use. All salts were dissolved in 1,2-dimethoxyethane (DME, Sigma-Aldrich), which was dehydrated over 4 Å molecular sieves for 1 week before use. Salt and solvent quantities were weighed on a microbalance inside an Ar-filled glove box (H_2O, $O_2 < 0.5$ ppm); electrolytes were freshly reformulated for every measurement.

Two-electrode measurements were performed in Swagelok-type cells (12 mm inner diameter), using ultrasmooth copper disks (10 mm diameter, 20 µm thickness, surface roughness < 0.1 µm) as the working electrode and mechanically cleaned flattened lithium foil (≈0.5 mm thickness, 10 mm diameter) as the counter electrode. A Celgard separator soaked with 40 µL of electrolyte was placed between the electrodes. Three-electrode measurements employed the same working and counter electrode materials with identical geometrical dimensions (total cell area 2.545 cm^2), separated by a Celgard–Whatman–Celgard stack soaked with 120 µL of electrolyte and incorporating a lithium reference electrode, allowing the working electrode (WE) and counter electrode (CE) responses to be measured independently.

2.2 | Galvanostatic and Impedance Electrochemical Test Protocols

Galvanostatic lithium plating/stripping was performed with a Biologic VSP-1 potentiostat using a modified Aurbach protocol comprising three stages [64–66]. In the pre-cycling stage, cells were held at open-circuit voltage for 1 h and then cycled five times between 0.01 and 1 V at 0.25 mA cm^{-2} to initiate interphase formation. In the lithium reservoir formation stage, 4 mAh cm^{-2} of lithium was deposited at 0.25 mA cm^{-2} and 2 mAh cm^{-2} was subsequently stripped at the same current density, leaving a nominal 2 mAh cm^{-2} reservoir. In the working stage, lithium was repeatedly plated and stripped (1 mAh cm^{-2} at 1 mA cm^{-2}) until a voltage cutoff of ±1 V was reached. All capacities and current densities were normalized to the geometric electrode area (0.785 cm^2 for the two-electrode cells). Under these conditions, the average Coulombic efficiency (CE_{avg}) is calculated as [64]

$$CE_{avg} = 1 - [(Q_{res} - Q_w)/n_{rev}Q_w] \times 100$$

where Q_{res} is the amount of lithium capacity of the reservoir, Q_w is the capacity exchange during each working cycle, and n_{rev} is the number of reversible cycles completed before the voltage cutoff is reached.

EIS was performed with the same potentiostat immediately after cell assembly and after each stage of the cycling protocol, using a 10 mV perturbation over the frequency range from 650 kHz to 0.15 Hz, centered on the voltage measured at the end of each stage. Prior to quantitative analysis, a Kramers–Kronig (K–K) test was applied to the measured spectra to assess data quality (typical residual errors of ≈10% on the imaginary component and ≈0.5% on the real component). K–K-validated spectra were fitted with the equivalent circuit $R_1(R_2Q_2)(R_3Q_3)(R_4Q_4)$, where R_1 is the bulk electrolyte resistance, R_2, R_3, and R_4 are interfacial resistances associated with processes occurring at progressively lower characteristic frequencies, and Q_2, Q_3, and Q_4 are constant-phase elements. Equivalent capacitances, $C_{eq,n}$, were derived from the fitted CPE parameters, and characteristic time constants were calculated as $\tau_n = R_n C_{eq,n}$.

2.3 | Raman and Nuclear Magnetic Resonance (NMR) Spectroscopy

Each formulated electrolyte was transferred, inside an Ar-filled glove box, into a sealed 1-mm-thick quartz cuvette and moved to the spectrometer in a sealed container; the cuvette was exposed to air only for the duration of acquisition. Raman spectra were collected using a Horiba Jobin–Yvon spectrometer equipped with a TRIAX 550 monochromator and a Symphony II liquid nitrogen-cooled CCD detector. A 633-nm laser source was attenuated to 4 mW using a 0.4 OD neutral density filter. Spectra were acquired with an instrumental resolution of approximately 2.6 cm^{-1}, using an acquisition time of 60 s and averaging three scans. Frequency calibration was performed against a cyclohexane standard, and intensities were normalized to the band at 1453 cm^{-1}. The S–N–S stretching region of the imide anions (700–770 cm^{-1}) and the conformational region of DME (780–905 cm^{-1}) were analyzed using constrained Lorentzian and Voigt line-shape models, respectively. The detailed fitting procedure, spectral assignments, constraints, and limitations are described in the Supporting Information.

^{1}H and ^{7}Li NMR spectra of each formulated electrolyte were acquired on a Bruker Avance III HD 600 MHz spectrometer using a coaxial configuration: A 2.5-mm inner tube containing 200 µL of DMSO-d_6 with 0.1% tetramethylsilane (TMS) was inserted into a 5-mm outer tube containing 400 µL of electrolyte. Following magnetic field shimming, spectra were acquired with standard pulse protocols. ^{1}H spectra were calibrated against the TMS resonance of the inner reference; ^{7}Li spectra were calibrated against an external standard of 1 M LiCl in D_2O, acquired immediately after each electrolyte measurement.

21960216, 2026, 21, Downloaded from https://chemistry-europe.onlinelibrary.wiley.com/doi/10.1002/celc.70331 by Politecnico Di Torino Sist. Bibl Del Polit Di Torino, Wiley Online Library on [02/11/2026]. See the Terms and Conditions (https://onlinelibrary.wiley.com/terms-and-conditions) on Wiley Online Library for rules of use; OA articles are governed by the applicable Creative Commons License

2.4 | Optical and Electron Microscopy

At selected steps of the cycling protocol, cells were disassembled inside an Ar-filled glove box (O_2, $H_2O < 0.5$ ppm) and the electrodes recovered. For macroscopic imaging, electrodes were transferred to the microscope, without air exposure, to a custom-built airtight optical sample holder and imaged immediately after cycling, using a Keyence (VHX-X1 series) digital microscope. Electrodes were then rinsed three times with pure DME and dried overnight in the glove box prechamber under dynamic vacuum. For scanning electron microscopy (SEM), electrodes were transferred without air exposure using a second custom-built airtight holder, and micrographs were collected at 15 kV acceleration voltage with a 30-µs dwell time at multiple magnifications. Energy-dispersive X-ray spectroscopy (EDX) elemental maps and single-point spectra were acquired on the same instrument.

3 | Results

3.1 | Electrolyte Formulations

The electrolyte matrix was designed to compare the effects of anion identity and anion combination while maintaining a constant total salt molality in the main formulation series. Six DME-based electrolytes with a total nominal Li^+ molality of 1 mol kg^{-1} were prepared: the single-salt formulations LiFSI (E1) and LiTFSI (E2); the equimolar binary mixtures LiFSI/LiTFSI (E3), LiFSI/$LiNO_3$ (E4), and LiTFSI/$LiNO_3$ (E5); and the equimolar ternary mixture LiFSI/LiTFSI/$LiNO_3$ (E6). This series enables lithium plating/stripping reversibility, interfacial impedance evolution, and deposit morphology to be compared as a function of anion composition without varying the overall salt content.

A complementary concentration series was prepared for spectroscopic analysis. Single-salt LiFSI and LiTFSI electrolytes were examined at 0.333, 0.5, and 1 mol kg^{-1}, together with an oversaturated $LiNO_3$/DME reference prepared from a nominal composition of 1 mol kg^{-1} (E7). These additional formulations were used to distinguish concentration-dependent changes in the Raman and NMR responses from those associated with the combination of different anions. The complete electrolyte compositions are shown in Table 1.

TABLE 1 | Composition of the investigated DME-based electrolytes (mol $kg^{-1}_{solvent}$).

Electrolyte	LiFSI	$LiNO_3$	LiTFSI
E1-033	0.333	—	—
E1-05	0.5	—	—
E1	1	—	—
E2-033	—	—	0.333
E2-05	—	—	0.5
E2	—	—	1
E3	0.5	—	0.5
E4	0.5	0.5	—
E5	—	0.5	0.5
E6	0.333	0.333	0.333
E7[a]	—	1	—

[a]Oversaturated solution.

3.2 | Lithium Reservoir Formation and Reversibility in Cu||Li Cells

The effect of electrolyte composition on lithium reservoir formation and durability was first assessed in Cu||Li cells using the modified Aurbach protocol described in Section 2.2. Unlike conventional Coulombic efficiency (CE) measurements, in which the electrode surface is continuously consumed and reconstructed during cycling, this protocol first establishes a well-defined lithium reservoir and subsequently probes its preservation during repeated plating and stripping. Representative voltage profiles are shown in Figure 1, while the corresponding number of reversible cycles, n_{rev}, and average Coulombic efficiency, CE_{avg}, are shown in Table S1.

Clear differences emerge between the nitrate-free and nitrate-containing formulations. Among the single-salt electrolytes, E2 shows particularly poor reservoir reversibility, reaching the voltage cutoff after only three reversible cycles and yielding a CE_{avg} of 66.66%. E1 performs better but remains limited to 23 cycles, with a CE_{avg} of 95.65%. Combining LiFSI and LiTFSI in E3 produces only a modest improvement, extending the response to 29 cycles and increasing CE_{avg} to 96.55%. By contrast, all nitrate-containing electrolytes sustain between 80 and 86 reversible cycles before consuming the Li reservoir and yield closely similar CE_{avg} values of 98.75%–98.84%. Under the present experimental conditions, nitrate incorporation in the electrolyte composition appears to be the common feature associated with markedly improved preservation of the lithium reservoir.

Although the nitrate-containing electrolytes E4–E6 display similar CE_{avg} values and cycle numbers (cf. Table S1), their voltage responses are not identical. E5 (LiTFSI/$LiNO_3$) develops a larger mean cell polarization during working stage cycling than E4 and E6, while the evolution of the end-of-stripping voltage follows a somewhat different trend. These differences are not reflected in CE_{avg} or in the reservoir lifetime, indicating that the voltage profile evolution provides complementary information on the electrochemical response of the different formulations. Because the two-electrode response includes contributions from both the working and counter electrodes, however, the origin of these differences cannot be assigned from the Cu||Li cell response alone.

Inspection of the reservoir formation step provides additional information on the early electrochemical response of the different systems. Most formulations exhibit a nucleation overvoltage close to −60 mV, with the exception of E2, for which a value of approximately −30 mV is observed. More pronounced differences appear during subsequent lithium growth: most electrolytes reach a deposition plateau near −10 mV, whereas E5 stabilizes at a somewhat larger absolute overvoltage of approximately −15 mV. The subsequent partial stripping profiles are comparatively similar across the electrolyte series. The clearest composition-dependent differences during reservoir formation therefore emerge during lithium growth rather than during the initial nucleation event or the first stripping step.

To distinguish the contributions of working and counter electrodes, the same reservoir protocol was subsequently applied

21960216, 2026, 21, Downloaded from https://chemistry-europe.onlinelibrary.wiley.com/doi/10.1002/celc.70331 by Politecnico Di Torino Sist. Bibl Del Polit Di Torino, Wiley Online Library on [02/11/2026]. See the Terms and Conditions (https://onlinelibrary.wiley.com/terms-and-conditions) on Wiley Online Library for rules of use; OA articles are governed by the applicable Creative Commons License

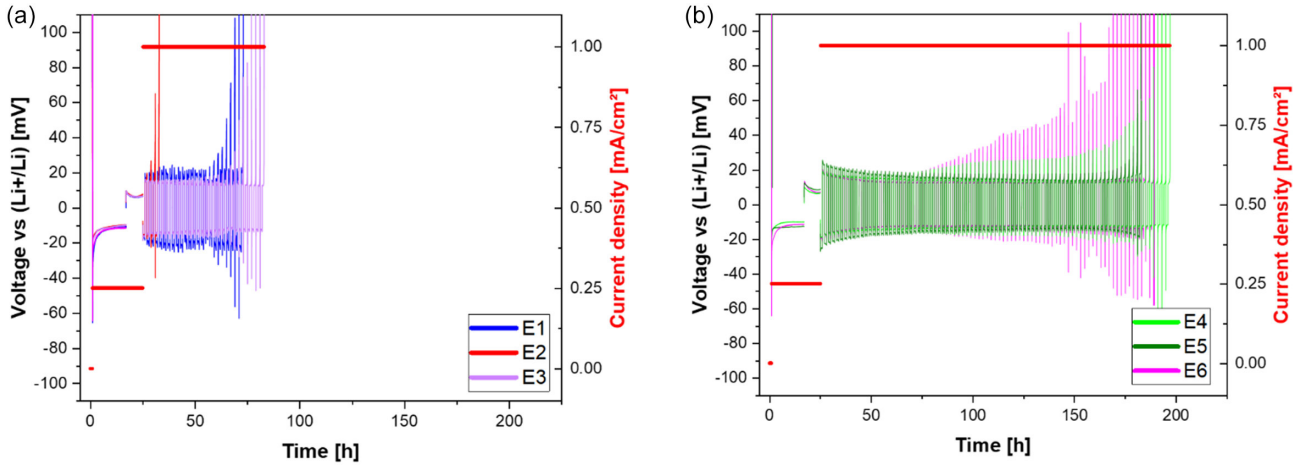

FIGURE 1 | Representative voltage profiles recorded during the modified Aurbach protocol [64–66] for Cu||Li cells containing (a) nitrate-free electrolytes E1–E3 and (b) nitrate-containing electrolytes E4–E6. The applied current density program is shown on the right axis.

in a three-electrode configuration containing a lithium reference electrode. Because this configuration differs from the two-electrode cells in electrode area, separator arrangement, and electrolyte volume, the absolute overpotentials cannot be compared directly between the two setups. Nevertheless, the principal qualitative trends are retained: nitrate-free electrolytes, and E2 in particular, show a rapid increase in polarization, whereas the nitrate-containing formulations maintain a substantially more stable working electrode response during cycling (Figure S1–S3).

The three-electrode measurements further show that the lithium counter electrode can contribute substantially to the overall Cu||Li voltage response, particularly during the early stages of cycling. For example, in E6 the counter electrode overpotential is larger than that of the working electrode during reservoir formation and remains appreciable during the first working cycles (Figure S3). Similar qualitative behavior is observed for the other nitrate-containing formulations. The larger overall cell polarization observed for E5 in the two-electrode configuration should therefore not be attributed exclusively to the Cu-supported lithium reservoir (for a qualitative comparison, see Figure S4). Indeed, the working electrode overpotentials of E4–E6 become comparatively similar during initial working cycles (Figure S1b). These results highlight the well-known importance of separating working electrode and counter electrode contributions when comparing electrolyte-dependent voltage responses [67].

Isolating the working electrode contribution also reveals differences among the nitrate-containing electrolytes that are not apparent from CE_{avg} or reservoir lifetime alone. As shown in Figure S5, E5 exhibits larger working electrode hysteresis and end-of-stripping polarization during the initial cycles, followed by a lower and comparatively stable response during extended cycling. E4 and E6 display different transient evolutions despite reaching similar reservoir lifetimes and average Coulombic efficiencies. These differences indicate that the nitrate-containing formulations follow distinct electrode-specific polarization pathways, but they do not establish a corresponding ranking in overall lithium reservoir reversibility.

3.3 | Interfacial Impedance Evolution During the Lithium Reservoir Formation Stage

EIS was used to follow the evolution of the electrode/electrolyte interfaces during lithium reservoir formation, first in the two-electrode Cu||Li configuration and subsequently in a three-electrode cell to distinguish the contributions of the Cu-supported lithium deposit and the lithium counter electrode. Spectra were recorded after each stage of the electrochemical protocol described in Section 2.2.

In the two-electrode cells, the initial response at open-circuit voltage is predominantly capacitive and highly resistive, consistent with the blocking behavior of the bare Cu working electrode combined with the contribution of the preexisting interface at the lithium counter electrode. Following pre-cycling, a broad interfacial contribution develops as electrochemical activity is established at the copper surface. Subsequent lithium deposition and partial stripping lead to a marked decrease in the overall impedance (Figures S6 and S7). This evolution is consistent with the formation of a larger electrochemically active surface upon lithium deposition, although changes in interphase transport and surface area effects cannot be separated in the two-electrode configuration.

At comparable stages of the protocol, the nitrate-free electrolytes E1–E3 generally show a lower absolute cell impedance than the nitrate-containing formulations E4–E6. The high-frequency intercept varies comparatively little across the electrolyte series, whereas larger composition-dependent differences occur in the interfacial response. The main differences among the formulations therefore arise predominantly from electrode/interfacial contributions rather than from the bulk Ohmic resistance. Because the two-electrode spectra contain contributions from both electrodes, however, these differences cannot be assigned to the Cu-supported lithium deposit alone.

To separate the electrode-specific contributions, the same reservoir formation protocol was repeated in a three-electrode cell containing a lithium reference electrode. At OCV, the Cu working electrode shows an almost purely capacitive response, whereas the lithium

21960216, 2026, 21, Downloaded from https://chemistry-europe.onlinelibrary.wiley.com/doi/10.1002/celc.70331 by Politecnico Di Torino Sist. Bibl Del Polit Di Torino, Wiley Online Library on [02/11/2026]. See the Terms and Conditions (https://onlinelibrary.wiley.com/terms-and-conditions) on Wiley Online Library for rules of use; OA articles are governed by the applicable Creative Commons License

counter electrode already exhibits a structured interfacial response associated with its preexisting passivated surface. After pre-cycling, a broad impedance contribution develops at the Cu working electrode, confirming its increasing contribution to the overall cell response (Figure S8). Absolute impedance values obtained in the two cell configurations cannot be compared directly because of differences in electrode area, separator arrangement, and electrolyte volume. Nevertheless, the high-frequency intercepts remain of comparable magnitude, while the main composition-dependent differences are retained in the interfacial region.

During lithium reservoir formation, the freshly deposited lithium at the working electrode exhibits a lower interfacial impedance than the lithium counter electrode (Figure 2). The counter electrode contribution also changes substantially between lithium deposition and the subsequent partial stripping step. Consequently, after lithium deposition, a substantial fraction of the impedance measured in the two-electrode configuration can originate from the lithium counter electrode, as suggested by the overall WE-CE impedance response of the three-electrode measurements (Figure S10). This observation is consistent with the electrode-specific voltage measurements discussed above and illustrates the difficulty of attributing the impedance response of Cu||Li cells exclusively to the freshly deposited lithium working electrode.

The working electrode spectra display a broad high-to-medium-frequency response together with a smaller low-frequency contribution. Both features remain clearly visible after deposition and partial stripping in the nitrate-free electrolytes, whereas the low-frequency contribution is markedly reduced, or nearly absent, in the nitrate-containing formulations. The effect of nitrate addition is therefore not simply a decrease in the absolute value of the interfacial impedance; rather, it changes the evolution and relative weight of the different relaxation processes associated with lithium deposition and stripping. To compare these changes quantitatively, the working electrode spectra were analyzed using an equivalent circuit model.

As the EIS spectra were acquired under nonideal conditions, their validity was assessed using a K–K test. Residual deviations were approximately 0.5% for the real component and reached approximately 10% for the imaginary component, with the largest deviations occurring in the medium-to-low-frequency region. Given the deviations observed in the K–K test, a quantitative interpretation of the low-frequency contribution was treated with particular caution.

In the Bode representation of the WE spectra (Figure S11), the high-to-medium-frequency region (10^3–10^6 Hz) can be resolved into at least two contributions, while an additional contribution appears at lower frequency. To provide a consistent comparative description without introducing an excessive number of fitting parameters, the spectra were fitted using the equivalent circuit $R_1(R_2Q_2)(R_3Q_3)(R_4Q_4)$. R_1 accounts for the Ohmic contribution, while the three R_nQ_n elements describe relaxation processes occurring at progressively lower characteristic frequencies. The corresponding equivalent capacitances $C_{eq,n}$ and characteristic time constants $\tau_n = R_n\, C_{eq,n}$ are shown in Tables 2, S2, and S3. In every case, the CPE exponents of the (R_2Q_2) and (R_3Q_3) loops were about 0.6–0.7 and 0.8–0.9, respectively.

Physical interpretation of the individual R_nQ_n contributions was guided by previous impedance studies of lithium electrodes [67–72], together with the fitted capacitance and characteristic frequency ranges. The higher-frequency R_2Q_2 contribution, characterized by equivalent capacitances in the low-microfarad range, is consistent with processes involving ion transport across the passivating interphase, which typically yields effective capacitances in the 10^{-6}–10^{-5} F range for thin SEI films. The intermediate-frequency R_3Q_3 contribution displays larger equivalent capacitances and is consistent with interfacial Faradaic processes that may include Li^+ desolvation and charge transfer. The lowest-frequency R_4Q_4 contribution is particularly sensitive to changes occurring during lithium removal, including changes in electrochemically active area and deposit connectivity. These assignments can be used as a phenomenological framework for comparing the electrolyte formulations, even though they should not be regarded as unique identification of the underlying elementary processes.

The fitted parameters (Tables 2, S2, and S3) reveal markedly different evolutions for the nitrate-free and nitrate-containing

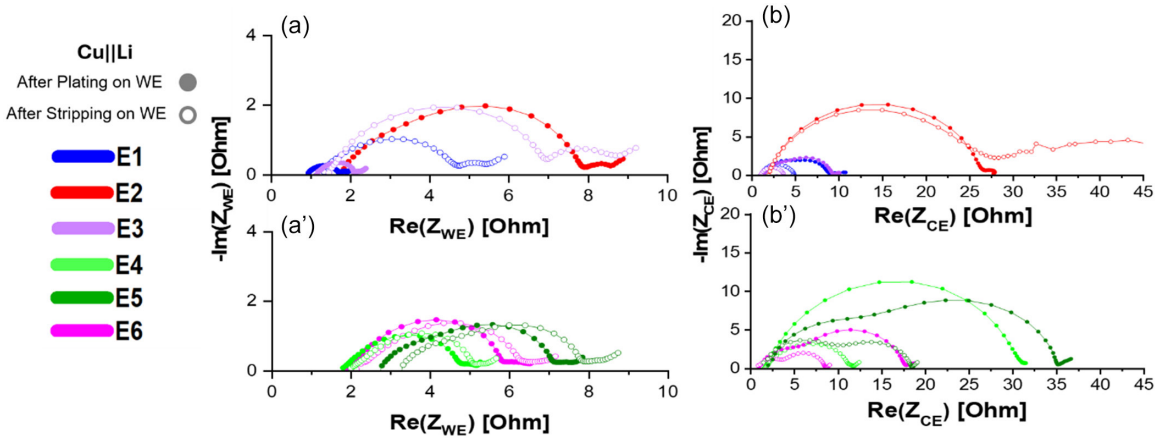

FIGURE 2 | Nyquist plots of the working electrode in the $LiNO_3$-free (a) and $LiNO_3$-containing (a') electrolyte, and the respective ones for the lithium counter electrode (b and b') after lithium deposition at the working electrode (filled symbols) and after the subsequent partial stripping step (open symbols).

21960216, 2026, 21, Downloaded from https://chemistry-europe.onlinelibrary.wiley.com/doi/10.1002/celc.70331 by Politecnico Di Torino Sist. Bibl Del Polit Di Torino, Wiley Online Library on [02/11/2026]. See the Terms and Conditions (https://onlinelibrary.wiley.com/terms-and-conditions) on Wiley Online Library for rules of use; OA articles are governed by the applicable Creative Commons License

TABLE 2 | Principal equivalent circuit fitting parameters for the high-to-medium frequency impedance response of the WE after plating (*Aft.plt.*) and stripping (*Aft.Strip.*) in each electrolyte composition.

	R_2, Ohm		R_3, Ohm		C_{eq2}, µF		C_{eq3}, µF	
Electrolyte	***Aft. plat.***	***Aft. strip.***	***Aft. plat.***	***Aft. strip.***	***Aft. plat.***	***Aft. strip.***	***Aft. plat.***	***Aft. strip.***
E1	0.36	1.36	0.45	2.04	32.67	8.54	50.39	26.13
E2	2.62	2.94	1.91	34.49	8.54	9.33	41.66	9.69
E3	0.42	3.21	0.48	2.31	17.18	11.40	62.57	39.43
E4	0.90	1.02	2.14	2.14	31.56	39.97	57.20	117.20
E5	2.04	2.15	2.34	2.45	8.98	8.70	80.07	98.90
E6	1.42	1.59	2.46	2.55	25.61	21.81	48.98	57.46

electrolytes. In E1 and E3, R_2 increases after partial stripping from 0.36 to 1.36 Ω and from 0.42 to 3.21 Ω, respectively, while C_{eq2} decreases. R_3 also increases in both formulations, although it remains comparatively low in absolute terms. E2 behaves differently: R_2 changes only slightly from 2.62 to 2.94 Ω, whereas R_3 increases sharply from 1.91 to 34.49 Ω, and C_{eq3} decreases from 41.66 to 9.69 µF. An even larger change is observed in the lowest-frequency contribution, for which R_4 increases from 1.01 to 261 Ω (Figures 2 and S9). This pronounced change in the medium- and low-frequency response is consistent with the severe interfacial deterioration accompanying the rapid reservoir failure observed for E2 (Figures 1a and S2).

By contrast, the nitrate-containing electrolytes show only limited changes in the fitted resistance values between the deposited and partially stripped states. For E4, E5, and E6, R_2 changes from 0.90 to 1.02 Ω, from 2.04 to 2.15 Ω, and from 1.42 to 1.59 Ω, respectively. Over the same step, R_3 also remains essentially unchanged at approximately 2–2.5 Ω. The C_{eq2} also shows comparatively small changes, whereas C_{eq3} increases to different extents depending on the salt combination. Importantly, the nitrate-containing formulations do not exhibit the pronounced increase in medium- and low-frequency resistance observed for the nitrate-free systems, particularly E2.

Taken together, the EIS results indicate that nitrate incorporation does not simply minimize the initial interfacial resistance. Instead, its clearest effect is the comparatively limited evolution of the working electrode impedance between lithium deposition and partial stripping. By contrast, the nitrate-free electrolytes show substantially larger changes in one or more interfacial contributions, with E2 displaying the most pronounced increase in both medium- and low-frequency resistance. The impedance evolution is therefore consistent with a more persistent electrochemically active interface in the nitrate-containing formulations during partial lithium removal. This behavior parallels their substantially longer lithium reservoir lifetime, although the equivalent circuit analysis alone does not identify the chemical origin of the improved interfacial response.

3.4 | Lithium Reservoir Morphology and Surface Elemental Distribution

The morphology of the lithium reservoir remaining on the copper working electrode after deposition of 4 mAh cm^{-2} and subsequent stripping of 2 mAh cm^{-2} was examined by optical microscopy and SEM. Samples were transferred without exposure to air using the procedures described in Section 2.4 and the airtight holders shown in Figure S12. The combined optical and SEM observations reveal pronounced differences depending on the electrolyte composition in deposit coverage, continuity, and characteristic morphology (Figures 3 and S13–S15).

At the macroscopic scale, all electrodes exhibit some degree of spatial heterogeneity, particularly near the edges of the copper substrate, where irregular and filamentous deposits are more frequently observed, consistent with the locally higher electric field arising from edge effects (Figure S13). Within this common pattern, the nitrate-free electrolytes E1–E3 produce less continuous coverage of the copper surface than the nitrate-containing formulations (Figure S13a–c). E1 and E2 display pronounced island-like deposits separated by exposed or poorly covered regions, with the most severe heterogeneity observed for E2. In this electrolyte, a substantial amount of detached lithium remained adhered to the separator during cell dismantling, leaving corresponding uncovered regions on the copper substrate (Figure S14c). E1 displays a denser population of smaller, moss-like deposits but no comparable accumulation of detached material on the separator (Figure S14a). The binary LiFSI/LiTFSI electrolyte E3 produces smoother and more extended deposits than either single-salt formulation, although localized clusters and small amounts of detached material remain visible near the electrode perimeter (Figure S14b).

In marked contrast, all nitrate-containing electrolytes E4–E6 yield substantially more continuous copper coverage and little evidence of material transfer to the separator. The remaining reservoirs display a more uniform metallic appearance, although differences among the three formulations remain visible. E4 and E5 show greater spatial heterogeneity and more clearly distinguishable surface features, whereas E6 produces the most homogeneous macroscopic coverage within the nitrate-containing series (Figure S13d–f).

The SEM images at different magnifications provide further insight into these differences (Figures 3 and S15, capturing the same regions as Figure S13). E1 forms compact, interconnected moss-like domains with characteristic dimensions of approximately 10 µm, locally covered by smoother surface debris and separated by rough grain boundaries (Figures 3a and S15a). E2 produces more discrete, approximately cylindrical, or

21960216, 2026, 21, Downloaded from https://chemistry-europe.onlinelibrary.wiley.com/doi/10.1002/celc.70331 by Politecnico Di Torino Sist. Bibl Del Polit Di Torino, Wiley Online Library on [02/11/2026]. See the Terms and Conditions (https://onlinelibrary.wiley.com/terms-and-conditions) on Wiley Online Library for rules of use; OA articles are governed by the applicable Creative Commons License

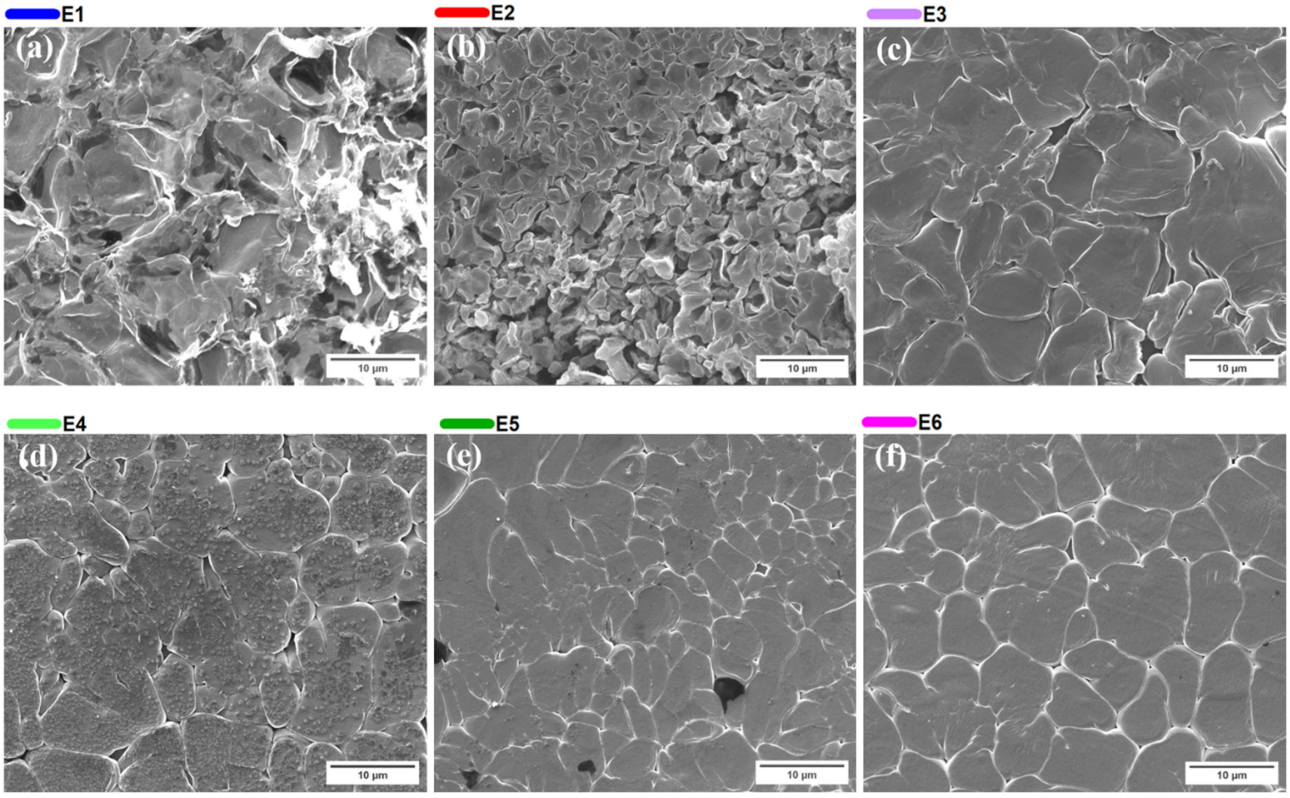

FIGURE 3 | Representative SEM images of the lithium reservoirs remaining on copper after deposition of 4 mAh cm^{-2} followed by stripping of 2 mAh cm^{-2} in electrolytes (a) E1, (b) E2, (c) E3, (d) E4, (e) E5, and (f) E6. Scale bars: 10 µm.

elongated deposits with a broad size distribution (Figures 3b and S15b). The material recovered from the separator displays a morphology resembling that remaining on the copper electrode (Figure S14e,f), with denser, finely structured regions and more damaged, entangled deposits elsewhere. E3 forms larger and smoother domains with greater lateral continuity than E1 and E2, although voids and local variations in connectivity remain apparent (Figures 3c and S15c).

A different morphology is observed for the electrolyte formulations containing lithium nitrate. Denser deposits with excellent lateral continuity are formed on the copper surface, with smoother and more rounded morphologies and discrete surface debris, especially in the case of E4 (Figures 3d and S15d). E5 displays a broader distribution of deposit sizes and closer lateral packing, although local voids and darker embedded regions remain visible (Figures 3e and S15e). E6 forms comparatively smooth, rounded domains with a narrower apparent size distribution and the most continuous packing of the series (Figures 3f and S15f). Surface debris is less prominent for E5 and E6 than for E4.

These morphological observations are consistent with the electrochemical response described previously (vide supra). The fragmented reservoir and extensive material detachment observed for E2 are consistent with its rapid loss of reversibility and the pronounced increase in low-frequency impedance during stripping. Conversely, the greater continuity of the nitrate-containing deposits is consistent with their improved reservoir preservation and more limited impedance evolution. The morphological differences among E4, E5, and E6 are nevertheless more pronounced than their differences in CE_{avg} and n_{rev}, indicating that deposit morphology alone does not determine electrochemical reversibility. These observations indicate that reservoir reversibility cannot be inferred from morphology alone and must also depend on the electrochemical properties and connectivity of the evolving interface.

EDX mapping of the nitrate-containing deposits reveals additional spatial heterogeneity in their surface elemental distribution (Figures S16–S18). Carbon and oxygen signals are more intense in the surface debris and along some of the boundaries between neighboring lithium domains, whereas fluorine, nitrogen, and sulfur are distributed more uniformly across the broader deposit regions. Single-point EDX spectra acquired from darker regions between deposits also show lower fluorine and sulfur content than those obtained from the surrounding surface.

These results demonstrate that the visible morphological features are accompanied by differences in surface elemental composition. However, the interaction volume of EDX, its relatively limited sensitivity to light elements, and the absence of chemical state information preclude the identification of specific SEI compounds or the assignment of a depth-resolved interphase structure. The carbon- and oxygen-rich regions may contain a larger contribution from solvent-derived decomposition products, whereas the more uniformly distributed fluorine-, nitrogen-, and sulfur-containing regions may include salt-derived species. These assignments remain tentative, however, and the EDX results are therefore considered only as phenomenological evidence of lateral compositional heterogeneity rather than as a direct determination of SEI composition.

21960216, 2026, 21, Downloaded from https://chemistry-europe.onlinelibrary.wiley.com/doi/10.1002/celc.70331 by Politecnico Di Torino Sist. Bibl Del Polit Di Torino, Wiley Online Library on [02/11/2026]. See the Terms and Conditions (https://onlinelibrary.wiley.com/terms-and-conditions) on Wiley Online Library for rules of use; OA articles are governed by the applicable Creative Commons License

3.5 | Raman Evidence for Composition-Dependent Ion Association and DME Coordination

Raman spectroscopy was used to examine changes in ion association and solvent coordination dependent on electrolyte composition through two complementary spectral regions: the S–N–S stretching modes of FSI and TFSI between 700 and 770 cm^{-1}, and the conformational modes of DME between 780 and 1050 cm^{-1}.

3.5.1 | Imide-Anion Coordination

Following established assignments [73, 74], the S–N–S stretching bands were deconvoluted into low-, intermediate-, and high-frequency contributions associated, respectively, with predominantly noncontact or solvent-separated anion environments (SSIP), direct Li^+–anion contact ion pair environments (CIP), more strongly associated or aggregated configurations (AGG). These components are used here as operational spectroscopic populations describing increasing degrees of Li^+–anion association rather than as uniquely defined molecular structures. In particular, the Raman spectra distinguish changes in the extent of contact association of the imide anions but do not uniquely determine the microscopic structure or stoichiometry of the corresponding coordination complexes.

The single-salt electrolytes reveal clear differences between the two imide anions (Figure 4 and Table S4). For LiTFSI, the fitted populations change only slightly between 0.333 and 1 mol kg^{-1}, with 81%–84% SSIP, 15%–18% CIP, and approximately 1% AGG. TFSI therefore remains predominantly in noncontact environments over the concentration range investigated. LiFSI shows a similarly limited concentration dependence, but a substantially larger contribution from contact-associated species, with 52%–54% SSIP, 34%–38% CIP, and 10%–12% AGG. These distributions are consistent with greater participation of FSI than TFSI in direct Li^+–anion association.

The binary LiFSI/LiTFSI electrolyte E3 differs from the corresponding 0.5 m single-salt references. Relative to E1-05, the FSI AGG fraction increases from 10% to 23%, while the SSIP and CIP fractions decrease from 54% to 48% and from 36% to 29%, respectively. By contrast, the TFSI distribution changes only slightly relative to E2-05, with an increase in SSIP from 82% to 85% and a decrease in CIP from 17% to 14%. This indicates that the coexistence of the two imide salts promotes higher-order association preferentially involving FSI while slightly reducing the participation of TFSI in contact-ion pairs.

The addition of $LiNO_3$ produces more pronounced changes in imide-anion distributions. In the LiTFSI/$LiNO_3$ electrolyte E5, the TFSI SSIP fraction increases from 82% in the corresponding 0.5 m single-salt reference to 91%, while its CIP fraction decreases from 17% to 8%. TFSI is therefore shifted toward predominantly noncontact-associated environments in the presence of nitrate. Conversely, the FSI distribution remains close to that of the corresponding 0.5 m single-salt reference E1-05, retaining a high CIP fraction of 39% and an AGG fraction of 7%. FSI consequently remains substantially involved in contact-associated environments despite the presence of nitrate.

The ternary electrolyte E6 displays the same qualitative distinction between the two imide anions. Relative to the corresponding 0.333 m single-salt references, the FSI population shifts toward greater association, with the AGG fraction increasing from 12% to 20% and the SSIP fraction decreasing from 54% to 42%. TFSI instead becomes more involved in SSIP species, with a decrease in CIP from 15 to 11%. The analysis of the imide band therefore shows that the response of FSI and TFSI to nitrate addition is markedly different: TFSI becomes less involved

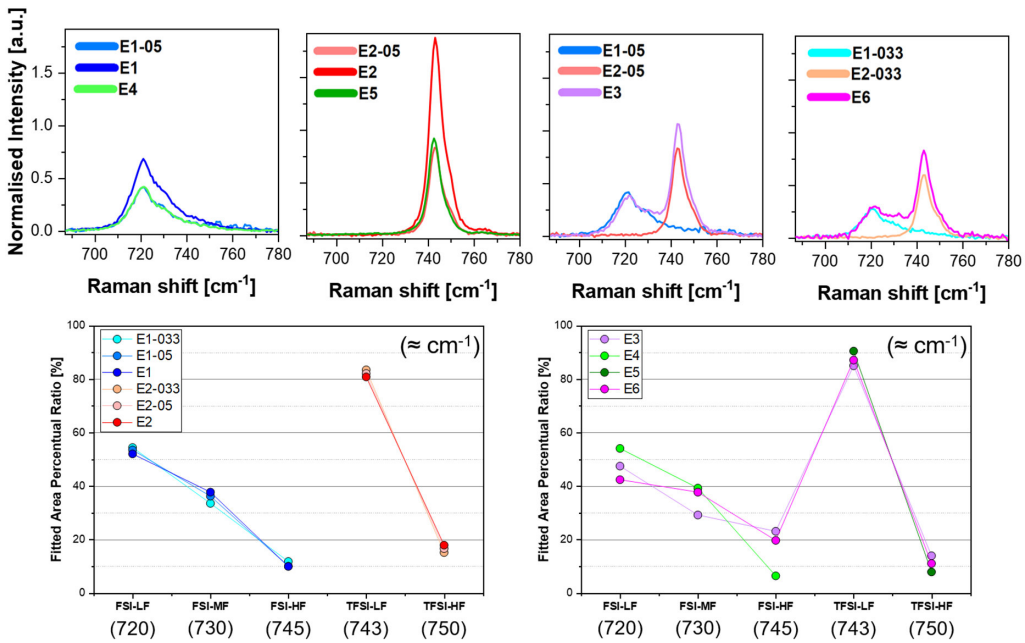

FIGURE 4 | Raman spectra of the S–N–S stretching mode of the imide salt in the relative electrolyte composition (upper panel) and relative percentage distribution calculated from the normalization of the fitted area (lower panels). LF, MF, and HF stand for low-, medium-, and high-frequency contributions, respectively.

21960216, 2026, 21, Downloaded from https://chemistry-europe.onlinelibrary.wiley.com/doi/10.1002/celc.70331 by Politecnico Di Torino Sist. Bibl Del Polit Di Torino, Wiley Online Library on [02/11/2026]. See the Terms and Conditions (https://onlinelibrary.wiley.com/terms-and-conditions) on Wiley Online Library for rules of use; OA articles are governed by the applicable Creative Commons License

in contact-associated configurations, whereas FSI retains, and in E6 even increases, its contribution to more strongly associated environments.

Because the S–N–S region probes only the imide anions, these observations do not directly determine nitrate occupancy within the Li^+ coordination environment. They nevertheless demonstrate a composition-dependent redistribution of imide-anion association upon $LiNO_3$ addition, which is considered below together with the DME Raman response and NMR results.

3.5.2 | DME Conformational Population

The DME conformational region provides complementary information about solvent participation in the Li^+ coordination environment. In fact, owing to its flexible ether backbone ($CH_3O–CH_2–CH_2–OCH_3$), DME exists in the liquid phase as several conformers, which are distinguished by their trans (T) and gauche (G/G′) dihedral sequences. At room temperature, the dominant conformers are TGT, TTT, TGG′, TGG, and TTG. Upon introduction of a lithium salt, this population is expected to reorganize toward the TGT and TGG conformations compatible with chelating coordination geometries around Li^+, at the expense of the other non-chelating forms [75–77].

Indeed, in agreement with previous literature assignments [75–77], in the 950–1050 cm^{-1} region, salt addition produces an increase of the relative intensity of the band near 1022 cm^{-1}, commonly associated with TGT-rich DME contributions, at the expense of the feature near 995 cm^{-1}, usually associated with the TTT-like conformations (Figure 5). This evolution is therefore consistent with a redistribution of the DME population toward folded geometries favored upon Li^+ coordination. The change is most evident for LiTFSI and less pronounced for LiFSI, while the multi-salt formulations display intermediate or composition-dependent responses. In the $LiNO_3$-containing electrolytes, an additional band appears near 1035 cm^{-1}, associated with the N–O stretching mode of nitrate.

More diagnostic, though more challenging to deconvolute is the 800–905 cm^{-1} region, which contains partially overlapping contributions from both free DME conformers and lithium-coordinated

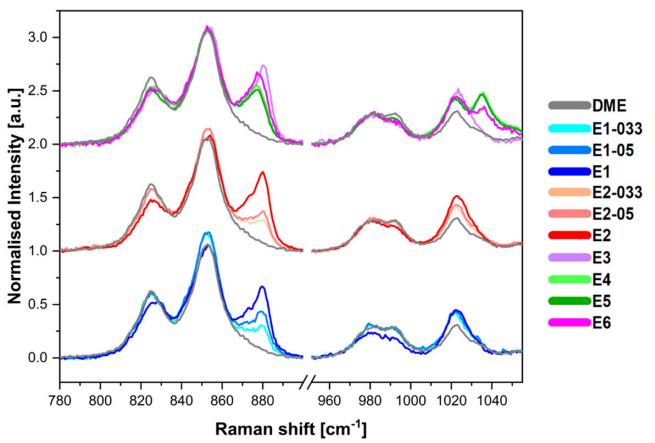

FIGURE 5 | Raman spectra of the DME region for the studied electrolyte compositions.

species. On the basis of the literature discussed in Note S1, the fitted components were therefore assigned operationally to free-DME and Li^+-perturbed DME contributions rather than to unique $[Li(DME)_x]^+$ molecular complexes. The fitted parameters are shown in Table S5.

At comparable salt molalities, the LiFSI solutions show a larger contribution from the low-frequency region, sensitive to the formation of coordinated entities, than the corresponding LiTFSI solutions, together with differences in the distribution of the free-DME conformational contributions (Figure S19). These observations indicate that FSI- and TFSI-containing electrolytes perturb the DME conformational ensemble differently.

To provide a common basis for comparison among spectra acquired and fitted under identical conditions, an apparent coordinated-DME descriptor, $n_{DME,app}$, was derived from the fitted Raman contributions (Table S6). This parameter is model dependent and is used only for relative comparison among the investigated electrolytes and should not be interpreted as an absolute Li^+ solvation number. The values do not vary monotonically with salt concentration. At 0.333 and 0.5 m, LiTFSI gives slightly higher values than LiFSI, whereas the two 1 m single-salt electrolytes give essentially identical values of 2.42–2.43. Among the 1 m formulations, E3 displays the highest $n_{DME,app}$ value, equal to 2.57, while the single-salt electrolytes E1 and E2 give values close to 2.4. The addition of lithium nitrate leads to lower values: E4 and E5 are characterized by $n_{DME,app} = 1.74$ and 1.55, respectively. The ternary electrolyte E6 does not follow this decrease, being characterized by $n_{DME,app} = 2.40$. The DME response to nitrate addition is therefore strongly dependent on the complete anion composition rather than on nitrate content alone.

E4 and E5 display the lowest $n_{DME,app}$ values of the series, with E5 giving the smallest value, whereas E6 retains a value comparable to the single-salt 1 m formulations. The differences among the E4–E6 electrolytes confirm that the effect of nitrate on the DME spectral response depends strongly on the accompanying imide anion and cannot be described by a single monotonic trend.

Taken together, the two Raman regions demonstrate a composition-dependent reorganization of both the imide-anion association and the DME spectral response. TFSI shifts toward predominantly noncontact-associated environments upon nitrate addition, whereas FSI retains a substantial contribution from contact-associated configurations. These differences are accompanied by non-monotonic variations in the coordination-sensitive DME bands. The combined Raman observations therefore demonstrate that the multi-salt formulations cannot be described as simple superpositions of the corresponding single-salt electrolytes. They are consistent with a redistribution of the Li^+ solvation ensemble as the anion composition changes, without uniquely determining the complete molecular composition of the primary Li^+ coordination shell.

3.6 | NMR Signatures of the Li^+ and DME Coordination Environments

To complement the Raman spectroscopy analysis, ^7Li and ^1H NMR were combined to probe the average environment of

21960216, 2026, 21, Downloaded from https://chemistry-europe.onlinelibrary.wiley.com/doi/10.1002/celc.70331 by Politecnico Di Torino Sist. Bibl Del Polit Di Torino, Wiley Online Library on [02/11/2026]. See the Terms and Conditions (https://onlinelibrary.wiley.com/terms-and-conditions) on Wiley Online Library for rules of use; OA articles are governed by the applicable Creative Commons License

the Li^+ cation and the response of the DME solvent, respectively. The spectra of the complete electrolyte series are shown in Figure S20. A single ^7Li resonance is observed for each electrolyte formulation. This behavior is consistent with a rapid exchange among the different Li^+ coordination environments on the NMR timescale, although the presence of several unresolved or rapidly interconverting species cannot be excluded. The chemical shifts should therefore be interpreted as composition-dependent averages rather than as signatures of individual coordination complexes.

In the single-salt solutions, the ^7Li resonance progressively shifts upfield with increasing salt molality, consistent with composition-dependent changes in the average Li^+ environment and shielding as ion association increases. At 0.333 and 0.5 m, the shift is slightly more pronounced for LiTFSI than for LiFSI. At 1 m, however, the resonances of E1, E2, and the binary LiFSI/LiTFSI electrolyte E3 converge within a relatively narrow range of around −1.3 ppm. Thus, although the two imide salts produce distinguishable average Li^+ environments at lower molality, these differences become substantially smaller in the 1 m formulations.

A more pronounced change is observed upon introduction of $LiNO_3$. The nitrate-containing electrolytes E4–E6 display ^7Li resonances shifted downfield relative to the nitrate-free 1 m formulations, with values of approximately −0.75 ppm for E4 and E5 and −1.00 ppm for E6. The supernatant recovered from the oversaturated $LiNO_3$/DME preparation E7 shows the most downfield resonance at approximately −0.08 ppm. Because the dissolved $LiNO_3$ concentration in this oversaturated reference could not be determined independently, E7 should be regarded as a qualitative nitrate-rich reference rather than as a quantitative 1 m solution. These results demonstrate that the presence of nitrate substantially modifies the average electronic and coordination environment experienced by Li^+. The ^7Li shifts alone do not establish the specific position or population of NO_3^- within the primary coordination shell. However, when considered together with the Raman results, the downfield displacement of the nitrate-containing formulations is consistent with nitrate contributing to the composition-dependent reorganization of the Li^+ coordination environment.

The ^1H resonances of the DME CH_2 and CH_3 groups provide complementary information on the average solvent environment. In the single-salt series, both resonances shift upfield relative to neat DME as the salt molality increases, with LiTFSI producing a larger displacement than LiFSI at comparable molality. The E3 resonances lie between those of the corresponding 1 m single-salt electrolytes, showing an approximately intermediate solvent response when FSI and TFSI coexist.

The effect of nitrate on the ^1H resonances is less pronounced than that observed by ^7Li NMR. E4 and E5 display chemical shifts close to those of the corresponding 0.5 m LiFSI and LiTFSI references, with only small additional displacements. E6 lies slightly downfield of E3 while remaining upfield of the dilute single-salt references, whereas E7 produces only a limited shift relative to neat DME. The solvent response therefore does not vary simply with nitrate content but depends on the complete salt composition.

Taken together, the ^7Li and ^1H NMR results provide complementary evidence of the reorganization of the electrolyte environment when the composition changes. The ^7Li resonance clearly distinguishes the nitrate-containing formulations from the nitrate-free imide electrolytes, while the ^1H shifts reveal more subtle changes in the average DME environment. These observations are consistent with the composition-dependent redistribution of ion association and solvent coordination inferred from Raman spectroscopy, although they do not provide well-defined individual anion populations within the primary Li^+ solvation shell.

4 | Discussion

The combined electrochemical, impedance, morphological, and spectroscopic results reveal two important effects of electrolyte composition on the global behavior. First, the introduction of $LiNO_3$ in electrolyte composition clearly separates E4–E6 from the nitrate-free formulations E1–E3. All nitrate-containing electrolytes preserve the lithium reservoir for 80–86 cycles, with CE_{avg} values close to 99%, while showing only limited changes in the working electrode impedance between lithium deposition and partial stripping at the beginning of the galvanostatic protocol. They also produce more continuous deposits with little evidence of detached lithium. By contrast, the nitrate-free electrolytes exhibit shorter reservoir lifetimes, greater evolution of the interfacial resistance during stripping, and less continuous lithium coverage. These convergent observations indicate that nitrate incorporation is the common compositional feature most clearly associated with improved reservoir preservation under the conditions investigated. Its presence does not minimize the initial interfacial resistance; rather, the nitrate-containing formulations exhibit a substantially more limited evolution of the working electrode interfacial response during partial lithium removal.

Second, the nature of the accompanying imide anion produces distinct changes in ion association and in the coordination-sensitive DME Raman response. Raman analysis shows that TFSI is predominantly present in noncontact environments and becomes even more strongly shifted toward SSIP-like configurations upon addition of $LiNO_3$. In E5, this evolution is accompanied by the lowest value of the Raman-derived apparent coordinated DME descriptor, $n_{DME,app}$. FSI shows a different behavior: It retains substantial CIP and AGG contributions in both E4 and E6, remaining significantly involved in contact-associated configurations in the presence of nitrate. The ternary formulation E6 combines increased association of FSI with reduced contact association of TFSI while retaining a $n_{DME,app}$ value comparable to those of the 1 m single-salt formulations. The response of the ternary system therefore cannot be described as a simple average of the corresponding binary electrolytes. More generally, the non-monotonic DME response across E4–E6 shows that nitrate addition does not produce a simple, composition-independent displacement of DME from the Li^+ coordination environment.

Importantly, the marked spectroscopic differences among E4, E5, and E6 do not translate into an equally marked ranking of reservoir reversibility. Their CE_{avg} values and cycle numbers remain closely similar, and three-electrode measurements show that the lithium counter electrode makes a substantial contribution to the overall cell polarization, including in E5. The larger two-electrode

21960216, 2026, 21, Downloaded from https://chemistry-europe.onlinelibrary.wiley.com/doi/10.1002/celc.70331 by Politecnico Di Torino Sist. Bibl Del Polit Di Torino, Wiley Online Library on [02/11/2026]. See the Terms and Conditions (https://onlinelibrary.wiley.com/terms-and-conditions) on Wiley Online Library for rules of use; OA articles are governed by the applicable Creative Commons License

polarization of E5 therefore cannot be interpreted as a direct measure of the behavior of its Cu-supported lithium reservoir. E6 produces the most homogeneous deposit morphology of the nitrate-containing series after lithium reservoir formation despite displaying spectroscopic characteristics that differ substantially from both E4 and E5. A direct relationship between a more homogeneous solvation ensemble and superior electrochemical performance therefore cannot be established from the present data. The most robust interpretation is instead that nitrate is the common compositional factor associated with improved reservoir preservation, whereas the coexisting imide anions modulate ion association, the solvent response, deposit morphology, and electrode-specific polarization without producing a correspondingly defined ranking in CE_{avg} or reservoir lifetime.

These observations support a picture in which the prereduction solvation ensemble depends on the complete salt composition and may influence the subsequent interfacial response. In a multi-salt electrolyte, the contribution of an anion to interfacial processes cannot be inferred simply from its bulk concentration because the different anions and solvent molecules participate in combined ion association and coordination equilibria. The combination of nitrate with the bulky, weakly coordinating TFSI produces a pronounced decrease in the contact-associated TFSI population, whereas FSI retains substantial CIP and AGG contributions when nitrate is present. These results establish that salt pairing modifies the relative association states of the imide anions. Recent literature calculations performed within a common computational framework also report different intrinsic Li^+–anion binding strengths for NO_3^-, FSI, and TFSI [78], with calculated values of −6.91, −6.01, and −5.67 eV for Li^+–NO_3^-, Li^+–FSI, and Li^+–TFSI, respectively. The weaker Li^+–TFSI interaction is thus consistent with the qualitative picture described above. These observations are also consistent with recent molecular dynamics simulations, corroborated experimentally, showing that the TFSI/NO_3^- ratio in mixed glyme electrolytes strongly affects both solvation structure and solvation dynamics [63].

These complementary observations, however, provide information on intrinsic association tendencies but do not directly determine the composition of the primary Li^+ coordination shell. They should therefore not be regarded as quantitative predictors of the coordination shell compositions, which also depend on solvent competition, ion aggregation, concentration, and collective interactions. Nevertheless, composition-dependent changes in these prereduction environments may in turn alter the relative availability and reactivity of electrolyte components during Li^+ desolvation and interfacial reduction as well as modify the reduction pathways involved in SEI formation [79].

This interpretation necessarily relies on a correlative approach. Raman spectroscopy directly probes changes in imide-anion association and in the coordination-sensitive DME spectral response, while the ^{7}Li and ^{1}H NMR shifts confirm that the average cation and solvent environments depend on the complete salt composition. Neither technique, however, provides a direct quantitative measurement of nitrate occupancy within the primary Li^+ coordination shell. Similarly, the limited impedance evolution and improved deposit continuity observed for E4–E6 demonstrate a more persistent electrochemical and morphological response during partial lithium removal but do not identify its chemical origin. In particular, the formation of SEI domains rich in Li_3N, LiN_xO_y, or LiF cannot be established from the present SEM/EDX and electrochemical measurements because direct chemical-state and depth-resolved characterization would be required. Similarly, the Cu||Li reservoir protocol employed here probes the formation and preservation of a finite lithium reservoir under controlled half-cell conditions and is not equivalent to an operational zero-excess full cell. The present results therefore establish correlations among electrolyte composition, spectroscopic response, lithium morphology, and interfacial evolution but are not sufficient to assign a unique molecular or interphase mechanism.

The proposed picture can be compared with two established approaches to controlling Li^+ coordination. In highly concentrated and localized high-concentration electrolytes [80, 81], extensive anion participation in the primary coordination shell is promoted mainly by reducing the relative availability of solvent molecules. Weakly solvating electrolytes achieve a related effect at conventional salt concentrations by using solvents with limited donor ability or steric constraints, thereby favoring anion coordination over solvent coordination [40, 41]. More recent electrolyte design concepts have further emphasized that cation–anion, anion–solvent, solvent–solvent, and higher-order interactions collectively determine the resulting solvation ensemble rather than acting as independent variables [42]. In particular, anion–solvent interactions have been identified as an additional means of tuning transport, desolvation, and interfacial chemistry [43], while multi-salt systems have been used to engineer cation–anion solvation through the simultaneous presence of chemically distinct anions [44]. In the present case, the total salt molality remains fixed at 1 mol kg^{-1} and DME is retained as the solvent; the principal variable is instead the identity and relative proportion of the coexisting anions. The observed redistribution of imide association and the nonadditive DME response therefore identify salt pairing as a complementary route for tuning the solvation ensemble at comparatively low total salt concentration. This interpretation is consistent with previous reports of improved lithium reversibility in multi-salt electrolytes [47–55], while indicating that their behavior cannot necessarily be understood as the simple superposition of independently acting salts.

From a design perspective, these findings suggest that the effectiveness of a functional anion depends not only on its presence in the electrolyte but also on how the complete salt composition modifies ion association and the solvent environment. In the present series, pairing nitrate with TFSI produces a pronounced shift of TFSI toward noncontact-associated configurations and a comparatively low $n_{DME,app}$, whereas FSI retains a greater degree of contact association. These differences do not, however, establish preferential nitrate occupancy quantitatively and do not translate into a simple ranking of reservoir reversibility. The broader implication is therefore not that one specific anion pair is universally optimal but that multi-salt electrolytes should be designed by considering the mutual effects of their constituent salts on ion association, solvent coordination, and interfacial response rather than treating their functions as independently additive. Salt pairing can thus provide an additional design variable for dilute electrolytes, complementary to increasing salt concentration or decreasing solvent coordinating strength. Its relevance to practical zero-excess architectures will require direct validation in cathode-limited full cells.

21960216, 2026, 21, Downloaded from https://chemistry-europe.onlinelibrary.wiley.com/doi/10.1002/celc.70331 by Politecnico Di Torino Sist. Bibl Del Polit Di Torino, Wiley Online Library on [02/11/2026]. See the Terms and Conditions (https://onlinelibrary.wiley.com/terms-and-conditions) on Wiley Online Library for rules of use; OA articles are governed by the applicable Creative Commons License

5 | Conclusion

The present study demonstrates that the behavior of low-concentration multi-salt electrolytes cannot be understood solely from the independent properties of their constituent salts. In 1 mol kg^{-1} DME electrolytes, the nitrate-containing formulations show markedly improved preservation of the lithium reservoir, with average Coulombic efficiencies close to 99%, limited evolution of the working electrode impedance during partial stripping, and more continuous lithium deposits. These effects are common to the nitrate-containing formulations E4–E6, despite their distinct voltage responses, deposit morphologies, and spectroscopic signatures.

Raman and $^{7}Li/^{1}H$ NMR spectroscopy further show that the accompanying imide anion modifies ion association and the DME and Li^{+} environments in the nitrate-containing formulations. TFSI is readily shifted toward noncontact configurations in the presence of $LiNO_3$, whereas FSI retains a substantial contribution from contact ion pair and aggregate configurations. The DME response also depends strongly on the complete anion composition and does not vary monotonically with nitrate content. The ternary electrolyte displays a nonadditive response, confirming that multi-salt solvation cannot be described as a simple superposition of the corresponding single-salt systems.

Overall, the results support a coordination-oriented interpretation in which the complete salt composition modifies ion association and the prereduction Li^{+} solvation ensemble, with corresponding changes in lithium deposition and interfacial evolution. Although the present data do not establish the quantitative population of the individual anions within the primary Li^{+} coordination shell or a direct causal relationship between solvation shell composition and specific SEI products, they identify salt pairing as a relevant design variable for dilute multi-salt electrolytes. The broader implication is that the salts contained in the electrolytes should not be considered as independently acting sources of interphase-forming species: Their mutual effects on ion association, solvent coordination, and interfacial response must also be taken into account. Salt pairing therefore provides a complementary strategy for tuning dilute electrolyte formulations without requiring an increase in total salt concentration.

Author Contributions

Andrea Gentile: investigation, data curation, formal analysis, visualization, writing – original draft. **Margherita Moreno**: conceptualization, supervision, validation, funding acquisition, writing – review and editing. **Sergio Brutti**: conceptualization, methodology, supervision, validation, funding acquisition, writing – review and editing. **Mauro Falconieri**: formal analysis, visualization, writing – review and editing. **Laure Monconduit**: supervision, validation, writing – review and editing. **Lorenzo Stievano**: conceptualization, methodology, supervision, validation, funding acquisition, writing – review and editing.

Acknowledgments

Financial support from the Ministero dell'Ambiente e della Sicurezza Energetica (MASE), through CSEA within the framework of the "Ricerca di Sistema Elettrico" program (Accordo di Programma), is gratefully acknowledged. Additional funding was provided by Sapienza University of Rome through projects RM123188F6EF1968, RM124190E9C10CE4, and RM125199C3C294 CD, and by the ANR through the Labex STORE-EX project (Grant ANR-10-LABX-76-01). The authors also warmly thank Flaminia Rondino and Serena Gagliardi (ENEA Casaccia) for their assistance with the acquisition and analysis of the Raman spectra.

Open access publishing facilitated by Politecnico di Torino, as part of the Wiley - CRUI-CARE agreement.

Funding

This study was supported by Agence Nationale de la Recherche (Labex STORE-EX, ANR-10-LABX-76-01), Ministero dell'Ambiente e della Sicurezza Energetica (Ricerca di Sistema Elettrico), and Sapienza Università di Roma (RM123188F6EF1968, RM124190E9C10CE4, RM125199C3C294CD).

Conflicts of Interest

The authors declare no conflicts of interest.

Data Availability Statement

The data that support the findings of this study are available from the corresponding author upon reasonable request.

References

1. J. Amici, P. Asinari, E. Ayerbe, et al., "A Roadmap for Transforming Research to Invent the Batteries of the Future Designed Within the European Large Scale Research Initiative BATTERY 2030+," *Advanced Energy Materials* 12(2022):2102785, https://doi.org/10.1002/aenm.202102785.

2. T. Wulandari, D. Fawcett, S. B. Majumder, and G. E. J. Poinern, "Lithium-Based Batteries, History, Current Status, Challenges, and Future Perspectives," *Battery Energy* 2(2023):20230030, https://doi.org/10.1002/bte2.20230030.

3. F. Degen, M. Winter, D. Bendig, and J. Tübke, "Energy Consumption of Current and Future Production of Lithium-Ion and Post Lithium-Ion Battery Cells," *Nature Energy* 8(2023):1284–1295, https://doi.org/10.1038/s41560-023-01355-z.

4. M. Burton, S. Narayanan, B. Jagger, et al., "Techno-Economic Assessment of Thin Lithium Metal Anodes for Solid-State Batteries," *Nature Energy* 10(2025):135–147, https://doi.org/10.1038/s41560-024-01676-7.

5. J. Liu, Z. Bao, Y. Cui, et al., "Pathways for Practical High-Energy Long-Cycling Lithium Metal Batteries," *Nature Energy* 4(2019):180–186, https://doi.org/10.1038/s41560-019-0338-x.

6. Z. Xie, Z. Wu, X. An, et al., "Anode-Free Rechargeable Lithium Metal Batteries: Progress and Prospects," *Energy Storage Materials* 32(2020):386–401, https://doi.org/10.1016/j.ensm.2020.07.004.

7. Y. Nikodimos, K. N. Shitaw, T. M. Hagos, et al., "Anode-Free Batteries: Pioneering Energy Storage Revolution," *Chemical Reviews* 126(2026):2391–2483, https://doi.org/10.1021/acs.chemrev.5c00533.

8. B. Liu, J.-G. Zhang, and W. Xu, "Advancing Lithium Metal Batteries," *Joule* 2(2018):833–845, https://doi.org/10.1016/j.joule.2018.03.008.

9. E. R. Cooper, M. Li, I. Gentle, Q. Xia, and R. Knibbe, "A Deeper Understanding of Metal Nucleation and Growth in Rechargeable Metal Batteries Through Theory and Experiment," *Angewandte Chemie International Edition* 62(2023):e202309247, https://doi.org/10.1002/anie.202309247.

10. A. Shao, X. Tang, M. Zhang, M. Bai, and Y. Ma, "Challenges, Strategies, and Prospects of the Anode-Free Lithium Metal Batteries," *Advanced Energy and Sustainability Research* 3(2022):2100197, https://doi.org/10.1002/aesr.202100197.

11. S. Stuckenberg, M. M. Bela, C.-T. Lechtenfeld, et al., "Influence of LiNO3 on the Lithium Metal Deposition Behavior in Carbonate-Based

21960216, 2026, 21, Downloaded from https://chemistry-europe.onlinelibrary.wiley.com/doi/10.1002/celc.70331 by Politecnico Di Torino Sist. Bibl Del Polit Di Torino, Wiley Online Library on [02/11/2026]. See the Terms and Conditions (https://onlinelibrary.wiley.com/terms-and-conditions) on Wiley Online Library for rules of use; OA articles are governed by the applicable Creative Commons License

Liquid Electrolytes and on the Electrochemical Performance in Zero-Excess Lithium Metal Batteries," *Small* 20(2024):2305203, https://doi.org/10.1002/smll.202305203.

12. J. Zheng, M. S. Kim, Z. Tu, S. Choudhury, T. Tang, and L. A. Archer, "Regulating Electrodeposition Morphology of Lithium: Towards Commercially Relevant Secondary Li Metal Batteries," *Chemical Society Reviews* 49(2020):2701–2750, https://doi.org/10.1039/c9cs00883g.

13. X.-R. Chen, B.-C. Zhao, C. Yan, and Q. Zhang, "Review on Li Deposition in Working Batteries: From Nucleation to Early Growth," *Advanced Materials* 33(2021):2004128, https://doi.org/10.1002/adma.202004128.

14. H. Adenusi, G. A. Chass, S. Passerini, K. V. Tian, and G. Chen, "Lithium Batteries and the Solid Electrolyte Interphase (SEI)—Progress and Outlook," *Advanced Energy Materials* 13(2023):2203307, https://doi.org/10.1002/aenm.202203307.

15. Z. Shadike, S. Tan, R. Lin, X. Cao, E. Hu, and X.-Q. Yang, "Engineering and Characterization of Interphases for Lithium Metal Anodes," *Chemical Science* 13(2022):1547–1568, https://doi.org/10.1039/d1sc06181j.

16. A. Mohammadi, P. Ghorbanzade, J. M. López del Amo, L. Monconduit, and L. Stievano, "From Formation to Reactivation of Inactive Lithium in Lithium Metal Anodes," *ChemElectroChem* 12(2025):e202500242, https://doi.org/10.1002/celc.202500242.

17. M. Abdollahifar and A. Paolella, ""Dead Lithium" Formation and Mitigation Strategies in Anode-Free Li-Metal Batteries," *Batteries & Supercaps* 8(2025):e202400505, https://doi.org/10.1002/batt.202400505.

18. B. Li, Y. Chao, M. Li, et al., "A Review of Solid Electrolyte Interphase (SEI) and Dendrite Formation in Lithium Batteries," *Electrochemical Energy Reviews* 6(2023):7, https://doi.org/10.1007/s41918-022-00147-5.

19. Z. Hu, G. Li, A. Wang, J. Luo, and X. Liu, "Recent Progress of Electrolyte Design for Lithium Metal Batteries," *Batteries Supercaps* 3(2020):331–335, https://doi.org/10.1002/batt.201900191.

20. H. Wan, J. Xu, and C. Wang, "Designing Electrolytes and Interphases for High-Energy Lithium Batteries," *Nature Reviews Chemistry* 8(2024):30–44,https://doi.org/10.1038/s41570-023-00557-z.

21. Y. S. Meng, V. Srinivasan, and K. Xu, "Designing Better Electrolytes," *Science* 3778(2022):6624, https://doi.org/10.1126/science.abq3750.

22. Q. Liu and L. Wang, "Fundamentals of Electrolyte Design for Wide-Temperature Lithium Metal Batteries," *Advanced Energy Materials* 13(2023):2301742, https://doi.org/10.1002/aenm.202301742.

23. C.-X. Xu, and J.-J. Jiang, "Designing Electrolytes for Lithium Metal Batteries With Rational Interface Stability," *Rare Metals* 40(2021):243–245, https://doi.org/10.1007/s12598-020-01629-5.

24. L. Dong, S. Zhong, B. Yuan, et al., "Electrolyte Engineering for High-Voltage Lithium Metal Batteries," *Research* 2022(2022):9837586, https://doi.org/10.34133/2022/9837586.

25. M. D. Tikekar, S. Choudhury, Z. Tu, and L. A. Archer, "Design Principles for Electrolytes and Interfaces for Stable Lithium-Metal Batteries," *Nature Energy* 1(2016):16114, https://doi.org/10.1038/nenergy.2016.114.

26. P. Xiao, X. Yun, Y. Chen, et al., "Insights Into the Solvation Chemistry in Liquid Electrolytes for Lithium-Based Rechargeable Batteries," *Chemical Society Reviews* 52(2023):5255–5316, https://doi.org/10.1039/D3CS00151B.

27. J. Liu, B. Yuan, L. Dong, et al., "Constructing Low-Solvation Electrolytes for Next-Generation Lithium-Ion Batteries," *Batteries Supercaps* 5(2022):e202200256, https://doi.org/10.1002/batt.202200256.

28. J.-X. Guo, W.-B. Tang, X. Xiong, et al., "Localized High-Concentration Electrolytes for Lithium Metal Batteries: Progress and Prospect," *Frontiers of Chemical Science and Engineering* 17(2023):1354–1371, https://doi.org/10.1007/s11705-022-2286-4.

29. X. Liu, A. Mariani, H. Adenusi, and S. Passerini, "Locally Concentrated Ionic Liquid Electrolytes for Lithium-Metal Batteries," *Angewandte Chemie International Edition* 62(2023):e202219318, https://doi.org/10.1002/anie.202219318.

30. X. Cao, H. Jia, W. Xu, and J.-G. Zhang, "Review—Localized High-Concentration Electrolytes for Lithium Batteries," *Journal of the Electrochemical Society* 168(2021):010522, https://doi.org/10.1149/1945-7111/abd60e.

31. G. Li, X. Duan, X. Liu, et al., "Locking Active Li Metal Through Localized Redistribution of Fluoride Enabling Stable Li-Metal Batteries," *Advanced Materials* 35(2023):2207310, https://doi.org/10.1002/adma.202207310.

32. A. Wang, T. Yang, L. Zhang, et al., "Origin of Solid Electrolyte Interphase Heterogeneity on Lithium Metal Anodes and Its Mitigation With Electrolyte Additives," *ACS Energy Letters* 10(2025):2727–2735, https://doi.org/10.1021/acsenergylett.5c00594.

33. S. Li, Z. Luo, L. Li, et al., "Recent Progress on Electrolyte Additives for Stable Lithium Metal Anode," *Energy Storage Materials* 32(2020):306–319, https://doi.org/10.1016/j.ensm.2020.07.008.

34. M. Nojabaee, D. Kopljar, N. Wagner, and K. A. Friedrich, "Understanding the Nature of Solid-Electrolyte Interphase on Lithium Metal in Liquid Electrolytes: A Review on Growth, Properties, and Application-Related Challenges," *Batteries & Supercaps* 4(2021):909–922, https://doi.org/10.1002/batt.202000258.

35. Y. Zhao, T. Zhou, L. P. H. Jeurgens, X. Kong, J. W. Choi, and A. Coskun, "Electrolyte Engineering for Highly Inorganic Solid Electrolyte Interphase in High-Performance Lithium Metal Batteries," *Chem* 9(2023):682–697, https://doi.org/10.1016/j.chempr.2022.12.005.

36. M. Li, X. Yang, D. Wu, et al., "Borate-Based Artificial Solid-Electrolyte Interphase Enabling Stable Lithium Metal Anodes," *ACS Applied Materials & Interfaces* 16(2024):66819–66825, https://doi.org/10.1021/acsami.3c11673.

37. L. Li, H. Dai, and C. Wang, "Electrolyte Additives: Adding the Stability of Lithium Metal Anodes," *Nano Select* 2(2021):16–36, https://doi.org/10.1002/nano.202000164.

38. J. Ma, *Liquid Electrolyte Chemistry for Lithium Metal Batteries: Design, Mechanisms, Strategies* (Wiley-VCH, 2022).

39. S. C. Kim, J. Wang, R. Xu, et al., "High-Entropy Electrolytes for Practical Lithium Metal Batteries," *Nature Energy* 8(2023):814–826, https://doi.org/10.1038/s41560-023-01280-1.

40. L. Liu, Z.-J. Chen, G.-Y. Zhu, et al., "A Review on Low-Concentration Electrolytes for Rechargeable Batteries," *Energy & Environmental Science* 18(2025):2668–2685, https://doi.org/10.1039/d4ee06096b.

41. X. Li, F. Luo, N. Zhou, et al., "Weakly Solvating Electrolytes for Lithium and Post-Lithium Rechargeable Batteries: Progress and Outlook," *Advanced Energy Materials* 15(2025):2501272, https://doi.org/10.1002/aenm.202501272.

42. J. Xu, "Electrolyte Design via Temperature-Responsive Solvation Structures for All-Climate Batteries," *Chemistry of Materials* 38(2026):4827–4838, https://doi.org/10.1021/acs.chemmater.5c03090.

43. J. Xu, V. Koverga, A. Phan, et al., "Revealing the Anion–Solvent Interaction for Ultralow Temperature Lithium Metal Batteries," *Advanced Materials* 36(2024):2306462, https://doi.org/10.1002/adma.202306462.

44. H. Zhang, Y. Zhao, X. Li, et al., "Wide-Temperature Electrolyte Design via Cation-Anion Solvation Engineering for 4.6 V Lithium-Ion Batteries," *Advanced Science* 12(2025);e03151, https://doi.org/10.1002/advs.202503151.

45. A. Hockmann, P. Yan, D. Diddens, I. Cekic-Laskovic, and M. Schönhoff, "Impact of the Anion Structure on Coordination and Dynamics in a Localized High-Concentration Battery Electrolyte," *Journal of Physical Chemistry B* 129(2025):6289–6299, https://doi.org/10.1021/acs.jpcb.5c01566.

21960216, 2026, 21, Downloaded from https://chemistry-europe.onlinelibrary.wiley.com/doi/10.1002/celc.70331 by Politecnico Di Torino Sist. Bibl Del Polit Di Torino, Wiley Online Library on [02/11/2026]. See the Terms and Conditions (https://onlinelibrary.wiley.com/terms-and-conditions) on Wiley Online Library for rules of use; OA articles are governed by the applicable Creative Commons License

46. R. Guo, X. Xu, S. Li, et al., "Elevating Operation Voltage of LiTFSI-Electrolyte via a Universal Passivation Strategy for High-Voltage Lithium-Metal Batteries," *Energy Storage Materials* 82(2025):104588, https://doi.org/10.1016/j.ensm.2025.104588.

47. R. Weber, M. Genovese, A. J. Louli, et al., "Long Cycle Life and Dendrite-Free Lithium Morphology in Anode-Free Lithium Pouch Cells Enabled by a Dual-Salt Liquid Electrolyte," *Nature Energy* 4(2019):683–689, https://doi.org/10.1038/s41560-019-0428-9.

48. H. Zheng, H. Xiang, F. Jiang, et al., "Lithium Difluorophosphate-Based Dual-Salt Low Concentration Electrolytes for Lithium Metal Batteries," *Advanced Energy Materials* 10(2020):2001440, https://doi.org/10.1002/aenm.202001440.

49. S. Liu, Q. Zhang, X. Wang, M. Xu, W. Li, and B. L. Lucht, "LiFSI and LiDFBOP Dual-Salt Electrolyte Reinforces the Solid Electrolyte Interphase on a Lithium Metal Anode," *ACS Applied Materials & Interfaces* 12(2020):33719–33728, https://doi.org/10.1021/acsami.0c08094.

50. Q. Wang, C. Zhao, J. Wang, et al., "High Entropy Liquid Electrolytes for Lithium Batteries," *Nature Communications* 14(2023):440, https://doi.org/10.1038/s41467-023-36075-1.

51. T. T. Beyene, H. K. Bezabh, M. A. Weret, et al., "Concentrated Dual-Salt Electrolyte to Stabilize Li Metal and Increase Cycle Life of Anode Free Li-Metal Batteries," *Journal of The Electrochemical Society* 166(2019):A1501–A1509, https://doi.org/10.1149/2.0731908jes.

52. X.-Q. Zhang, X. Chen, L.-P. Hou, et al., "Regulating Anions in the Solvation Sheath of Lithium Ions for Stable Lithium Metal Batteries," *ACS Energy Letters* 4(2019):411–416, https://doi.org/10.1021/acsenergylett.8b02376.

53. I. Phiri, J. Kim, D.-H. Oh, et al., "Synergistic Effect of a Dual-Salt Liquid Electrolyte With a LiNO 3 Functional Additive Toward Stabilizing Thin-Film Li Metal Electrodes for Li Secondary Batteries," *ACS Applied Materials & Interfaces* 13(2021):31605–31613, https://doi.org/10.1021/acsami.1c04972.

54. L. Zheng, F. Guo, T. Kang, et al., "Stable Lithium-Carbon Composite Enabled by Dual-Salt Additives," *Nano-Micro Letters* 13(2021):31613, https://doi.org/10.1007/s40820-021-00633-3.

55. H. Zhang, Y. Lin, and J. Wang, "Design of Localized High-Concentration Electrolytes From the Perspective of Physicochemical Properties," *Journal of Physical Chemistry Letters* 15(2024):8378–8386, https://doi.org/10.1021/acs.jpclett.4c01613.

56. X. Zhao, Z. Fu, X. Zhang, et al., "More Is Better: High-Entropy Electrolyte Design in Rechargeable Batteries," *Energy & Environmental Science* 17(2024):2406–2430, https://doi.org/10.1039/d3ee03821a.

57. P. Luo, Y. Zhang, J. Song, et al., "Ternary-Salt Localized High-Concentration Electrolyte: An Ideal Companion Facilitating Stable High-Voltage Cycling of Lithium Metal Batteries," *Journal of Energy Storage* 102(2024):114197, https://doi.org/10.1016/j.est.2024.114197.

58. T. T. Beyene, W.-N. Su, and B. J. Hwang, "Dilute Dual-Salt Electrolyte for Successful Passivation of In-Situ Deposited Li Anode and Permit Effective Cycling of High Voltage Anode Free Batteries," *Journal of Power Sources* 542(2022):231752, https://doi.org/10.1016/j.jpowsour.2022.231752.

59. V. A. Afrifah, J. M. Kim, Y. M. Lee, I. Phiri, Y.-G. Lee, and S.-Y. Ryou, "Synergistic Effects Between Dual Salts and Li Nitrate Additive in ether Electrolytes for Li-Metal Anode Protection in Li Secondary Batteries," *Journal of Power Sources*. (548(2022):232017, https://doi.org/10.1016/j.jpowsour.2022.232017.

60. M. Wang, Q. Sun, Y. Liu, et al., "Impact of Lithium Nitrate Additives on the Solid Electrolyte Interphase in Lithium Metal Batteries," *Chinese Journal of Structural Chemistry* 43(2024):100203, https://doi.org/10.1016/j.cjsc.2023.100203.

61. H. Yu, W. Deng, Z. Ding, et al., "Advanced Anode-Free Lithium Metal Batteries Enabled by Low-Concentration Dual-Salt Electrolyte," *Journal of Power Sources* 666(2026):239114, https://doi.org/10.1016/j.jpowsour.2025.239114.

62. Q. Wang, C. Zhao, Z. Yao, et al., "Entropy-Driven Liquid Electrolytes for Lithium Batteries," *Advanced Materials* 35(2023):2210677, https://doi.org/10.1002/adma.202210677.

63. E. Rems, T. Šlosar, S. Drvarič Talian, M. Huš, R. Dominko, and A. Serva, "Strongly vs. Weakly Associating Anions: Transport–Structure Relationship in LiTFSI–LiNO3 Electrolytes," *Physical Chemistry Chemical Physics* 27(2025):22082–22092, https://doi.org/10.1039/d5cp02750k.

64. A. Mohammadi, S. Djafer, S. Sayegh, et al., "Assessing Coulombic Efficiency in Lithium Metal Anodes," *Chemistry of Materials* 35(2023):2381–2393, https://doi.org/10.1021/acs.chemmater.2c03518.

65. B. D. Adams, J. Zheng, X. Ren, W. Xu, and J.-G. Zhang, "Accurate Determination of Coulombic Efficiency for Lithium Metal Anodes and Lithium Metal Batteries," *Advanced Energy Materials* 8(2018):1702097, https://doi.org/10.1002/aenm.201702097.

66. D. Aurbach, O. Youngman, and P. Dan, "The Electrochemical Behavior of 1,3-Dioxolane—LiClO4 Solutions—II. Contaminated Solutions," *Electrochimica Acta* 35(1990): 639–655, https://doi.org/10.1016/0013-4686(90)87056-8.

67. A. Mohammadi, L. Monconduit, L. Stievano, and R. Younesi, "Measuring the Nucleation Overpotential in Lithium Metal Batteries: Never Forget the Counter Electrode!," *Journal of the Electrochemical Society* 169(2022):070509, https://doi.org/10.1149/1945-7111/ac7e73.

68. D. Aurbach and A. Zaban, "Impedance Spectroscopy of Lithium Electrodes: Part 3. The Importance of Li Electrode Surface Preparation," *Journal of Electroanalytical Chemistry* 365(1994):41–45, https://doi.org/10.1016/0022-0728(93)02999-X.

69. S. Drvarič Talian, J. Bobnar, A. R. Sinigoj, I. Humar, and M. Gaberšček, "Transmission Line Model for Description of the Impedance Response of Li Electrodes With Dendritic Growth," *The Journal of Physical Chemistry C* 123(2019):27997–28007, https://doi.org/10.1021/acs.jpcc.9b05887.

70. F. Single, B. Horstmann, and A. Latz, "Theory of Impedance Spectroscopy for Lithium Batteries," *Journal of Physical Chemistry C* 123(2019):27327–27343, https://doi.org/10.1021/acs.jpcc.9b07389.

71. S. D. č. Talian, S. Brutti, M. A. Navarra, J. Moškon, and M. Gaberscek, "Impedance Spectroscopy Applied to Lithium Battery Materials: Good Practices in Measurements and Analyses," *Energy Storage Materials* 69(2024):103413, https://doi.org/10.1016/j.ensm.2024.103413.

72. A. Zaban, E. Zinigrad, and D. Aurbach, "Impedance Spectroscopy of Li Electrodes. 4. A General Simple Model of the Li−Solution Interphase in Polar Aprotic Systems," *Journal of Physical Chemistry* 100(1996):3089–3101, https://doi.org/10.1021/jp9514279.

73. D. M. Seo, P. D. Boyle, R. D. Sommer, J. S. Daubert, O. Borodin, and W. A. Henderson, "Solvate Structures and Spectroscopic Characterization of LiTFSI Electrolytes," *Journal of Physical Chemistry B* 118(2014):13601–13608, https://doi.org/10.1021/jp505006x.

74. S.-D. Han, R. D. Sommer, P. D. Boyle, et al., "Electrolyte Solvation and Ionic Association: Part IX. Structures and Raman Spectroscopic Characterization of LiFSI Solvates," *Journal of the Electrochemical Society* 169(2022):110544, https://doi.org/10.1149/1945-7111/ac9a07.

75. O. Holin, Y. Gofer, D. T. Major, and D. Aurbach, "Understanding the Unique Thermodynamic Behavior of MgTFSI2/DME Solutions. Part 2: Thermodynamic Hypothesis, Raman Analyses, and Driving Forces," *Journal of Physical Chemistry C* 75(2023):14863–14873, https://doi.org/10.1021/acs.jpcc.3c01476.

76. N. Goutev, K. Ohno, and H. Matsuura, "Raman Spectroscopic Study on the Conformation of 1,2-Dimethoxyethane in the Liquid Phase and in Aqueous Solutions," *Journal of Physical Chemistry A* 104(2000):9226–9232, https://doi.org/10.1021/jp001340+.

77. Y. Ogawa, M. Ohta, M. Sakakibara, H. Matsuura, I. Harada, and T. Shimanouchi, "Vibration Spectra and Rotational Isomerism of

21960216, 2026, 21, Downloaded from https://chemistry-europe.onlinelibrary.wiley.com/doi/10.1002/celc.70331 by Politecnico Di Torino Sist. Bibl Del Polit Di Torino, Wiley Online Library on [02/11/2026]. See the Terms and Conditions (https://onlinelibrary.wiley.com/terms-and-conditions) on Wiley Online Library for rules of use; OA articles are governed by the applicable Creative Commons License

Chain Molecules. V. 2,5-Dioxahexane, 2,5-Dithiahexane, and 2-Oxa-5-thiahexane," *Bulletin of the Chemical Society of Japan* 50(1977): 650–660, https://doi.org/10.1246/bcsj.50.650.

78. A. Chen, J. Wang, W. Yang, et al., "De-Solvation of Heteroalkali Cations Enabling Stable Solid Electrolyte Interphase for Dendrite-Free Lithium Metal Batteries," *Nature Communications* 16(2025):11400, https://doi.org/10.1038/s41467-025-66197-7.

79. Y. Wu, G. Ge, S. Wang, L. Xiong, and Z. He, "Formation Mechanisms of Solid Electrolyte Interphase and Its Influence on Lithium Battery Performance," *Materials Today Energy* 54(2025):102124, https://doi.org/10.1016/j.mtener.2025.102124.

80. J. Qian, W. A. Henderson, W. Xu, et al., "High Rate and Stable Cycling of Lithium Metal Anode," *Nature Communications* 6(2015):6362, https://doi.org/10.1038/ncomms7362.

81. L. Suo, Y.-S. Hu, H. Li, M. Armand, and L. Chen, "A New Class of Solvent-in-Salt Electrolyte for High-Energy Rechargeable Metallic Lithium Batteries," *Nature Communications* 4(2013):1481, https://doi.org/10.1038/ncomms2513.

Supporting Information

Additional supporting information can be found online in the Supporting Information section.

21960216, 2026, 21, Downloaded from https://chemistry-europe.onlinelibrary.wiley.com/doi/10.1002/celc.70331 by Politecnico Di Torino Sist. Bibl Del Polit Di Torino, Wiley Online Library on [02/11/2026]. See the Terms and Conditions (https://onlinelibrary.wiley.com/terms-and-conditions) on Wiley Online Library for rules of use; OA articles are governed by the applicable Creative Commons License